Topology of SmB_6 revisited by means of topological quantum chemistry

Mikel Iraola,[1,2,*] Iñigo Robredo,[1,3] Titus Neupert,[4] Juan L. Mañes,[5] Roser Valentí,[6,†] and Maia G. Vergniory[1,3,‡]

[1]*Donostia International Physics Center, 20018 Donostia-San Sebastian, Spain*

[2]*Institute for Theoretical Solid State Physics, IFW Dresden, Helmholtzstrasse 20, 01069 Dresden, Germany*

[3]*Max Planck Institute for Chemical Physics of Solids, 01187 Dresden, Germany*

[4]*Department of Physics, University of Zürich, Winterthurerstrasse 190, CH-8057 Zürich, Switzerland*

[5]*Department of Physics, University of the Basque Country UPV/EHU, Apartado 644, 48080 Bilbao, Spain*

[6]*Institut für Theoretische Physik, Goethe-Universität Frankfurt, 60438 Frankfurt am Main, Germany*

(Received 18 December 2023; accepted 5 June 2024; published 20 August 2024)

The mixed-valence compound SmB_6 with partially filled samarium $4f$ flat bands hybridizing with $5d$ conduction bands is a paramount example of a correlated topological heavy-fermion system. In this study, we revisit the topology of SmB_6 within the formalism of topological quantum chemistry and symmetry-based indicators. Based on this approach, we reach a detailed classification of the material's topology, and we reformulate the origin of topology in terms of band representations. We corroborate these aspects by constructing a minimal TB model that is consistent with all the symmetries of the system and is able to reproduce the topology of the material. We finally unveil the previously overlooked formation of multiple topological gaps, and we discuss its implications for experiments.

DOI: 10.1103/PhysRevResearch.6.033195

I. INTRODUCTION

Due to the presence of correlated electrons and a complex electronic structure, the number of heavy-fermion materials predicted as topological is still scarce [1–5]. Heavy-fermion materials [6–10] are intermetallic compounds of lanthanides and actinides with localized f and dispersive d bands near the Fermi surface. A most discussed type of heavy-fermion material are Kondo insulators [6,7], which undergo a transition into a paramagnetic insulating phase when the temperature is lowered below a critical value. Importantly, while these materials are strongly interacting electron systems, their ground states and excitations can be described in terms of highly renormalized f electrons that hybridize with conduction electrons to form a filled band of quasiparticles [11,12]. Alternatively, if the mean occupation of the f orbitals is not close to an integer value, the systems may be classified as mixed valent. Even though both kinds of systems have been intensively analyzed during the last decades and preliminary research has been done towards a general understanding of their topological properties [13–17], there is still a lack of a methodology for the general classification of topological phases in heavy fermion insulators. This lack of methodology might be one of the reasons why the identification of bulk topological heavy-fermion insulators has not been very successful so far.

In this work, we revisit the topology of SmB_6 in terms of topological quantum chemistry (TQC) [18–20] and symmetry indicators [21–23] via density functional theory (DFT) calculations. Both, experimental and theoretical studies have labeled this system as a mixed-valence insulator [24–29]. Moreover, experimental analyses have found evidences of surface phenomena which were interpreted as signatures of the presence of topological boundary states [30–34]. These observations are compatible with theoretical analyses which classify SmB_6 as a strong topological insulator [13,25,35–37]. Further studies have identified SmB_6 as a material hosting a mirror-Chern insulating phase, and they have studied the manifestation of this nontrivial topology in the surface-state spin textures of the crystal [38,39]. Our analysis has led us to a refined topological classification that considers all crystal symmetries on an equal footing. We also discuss the origin of topology in terms of the interplay between band representations induced from Sm $4f$ and $5d$ states, and we report the presence of multiple topological gaps close to the Fermi surface. In addition, we construct a minimal effective tight-binding (TB) model able to reproduce the topology of *ab initio* bands. Based on this model, we simulate the in-gap surface states of the crystal in a slab geometry, and we corroborate the features of crystalline topology.

We note that our approach is based on a single-particle picture of renormalized states, rather than on a multiplet description [25,28,40]. Although these two descriptions are fundamentally different, in the case of SmB_6 the symmetry properties of states close to zero energy are identical in both approaches. As we explain in detail in Appendix A, this is due to the fact that the low-energy region of the spectrum of

*Contact author: m.iraola@ifw-dresden.de

†Contact author: valenti@itp.uni-frankfurt.de

‡Contact author: maia.vergniory@cpfs.mpg.de

binding energies is dominated by transitions from a singlet to states where the $4f$ shell of Sm is two electrons short from half-filling. Moreover, previous analyses perfomed via numerical methods beyond DFT regarding the implementation of electron interactions suggest that the topology of single-particle excitations in SmB_6 can be described effectively in terms of a quasiparticle picture (see Appendix B for a more detailed discussion on the effect of interactions). These facts encouraged us to analyze this material in terms of TQC and symmetry indicators of topology within the DFT framework, and might inspire the application of this approach to other heavy-fermion materials with similar properties.

We have structured the paper in the following way. In Sec. II, we analyze the general features of the band structures of heavy-fermion insulators from the perspective of TQC, and we describe the way in which the hybridization between f and d bands might lead to topological phases. Section III contains a discussion on the possibility of having multiple cumulative topological bands close to the Fermi level in a range accessible to experimental probes. In Sec. IV, we revisit the topological classification of SmB_6, and we investigate whether this material is a candidate to exhibit in-gap boundary states close to the Fermi level. Finally, in Sec. V, we present the conclusions and outlook of our work.

II. HYBRIDIZATION-DRIVEN TOPOLOGY IN HEAVY-FERMION INSULATORS

A set of orbitals is closed if they span a single-particle Hilbert space invariant under the action of the space group of the crystal. From a closed set of orbitals, one can extract a basis for an infinite-dimensional representation of the space group known as *band representation* [41–43]. The band representation can then be used to describe the transformation properties of bands induced by changing to a basis of Bloch-like combinations of the orbitals. An *atomic limit* is associated to a set of bands transforming as a band representation (in reciprocal space). Furthermore, a band representation that cannot be split into smaller band representations is dubbed an *elementary band representation* (EBR).

According to the formalism of topological quantum chemistry [18–20], if a set of bands does not have an atomic limit, it is topological. Showing that the representation of a set of bands is not a band representation is then sufficient to demonstrate that they are topological bands. When this topology is visible to crystal symmetries, it can be inferred from little group irreducible representations (irreps) of bands at maximal $\boldsymbol{k}$ points of the Brillouin zone (BZ): if this set of irreps does not coincide with those of any linear combination of EBRs with non-negative integer coefficients, the bands are not related to an atomic limit, and their topology is necessarily nontrivial.

A remarkable feature of mixed valence and (magnetically nonordered) Kondo insulators containing lanthanide elements is that the low-energy region of their band structure is dominated by the presence of dispersive and heavy bands. In terms of atomic limits, heavy bands transform as a band representation ρ_f induced from localized $4f$ orbitals of the lanthanide element, while the band representation ρ_d of dispersive bands is induced from spatially extended $5d$ orbitals of the same element. The hybridization between $4f$ and $5d$ orbitals plays an important role in heavy-fermion insulators since it is responsible for the fluctuating occupation of $4f$ orbitals. When the average occupation of these states is close to an integer value, the system tends to exhibit Kondo behavior, and to become a Kondo insulator below a given critical temperature. In contrast, if the average occupation corresponds to an intermediate value between two integers, the compound is a mixed-valence material. The system might, in both cases, have an electronic structure that can be described in terms of renormalized heavy and dispersive bands, in the absence of magnetic ordering [44]. We set the focus of our discussion on such phases.

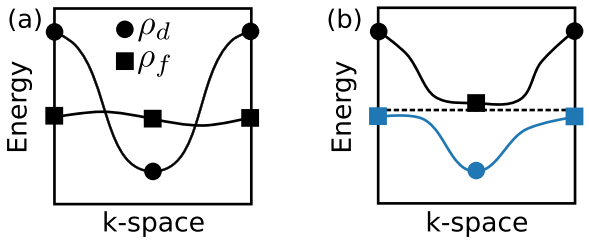

FIG. 1. Schematic representation of the way the hybridization between f and d bands leads to a heavy-fermion insulator. Circles and squares denote little-group irreps corresponding to ρ_d and ρ_f, respectively. (a) Band structure if the hybridization were not present. (b) Case with hybridization, where a spectral gap separates valence (blue) and conduction (black) bands. Depending on the material, differentiating between irreps of ρ_f and ρ_d might not be possible once the hybridization is considered.

The hybridization and spin-orbit coupling (SOC) mediated interplay of $4f$ and $5d$ bands might lead to a nontrivial topology. Although the hybridization cannot be tuned arbitrarily in a given material, it will be helpful to consider here that we can switch it on and off in order to gain insight into the interplay between dispersive and heavy bands. We consider as starting point the band structure represented schematically in Fig. 1(a), where the bundle of heavy $4f$ bands intersects the set of dispersive $5d$ bands. Before considering the hybridization, it is possible to assign every irrep to either ρ_f or ρ_d, even when those representations have some irreps in common. Furthermore, the Fermi level would typically lie on the bundle of intersecting f and d bands, and the system would be a metal. When the hybridization is turned on, a gap opens between valence and conduction bands and the system becomes an insulator, while some irreps are exchanged between ρ_d and ρ_f. According to TQC, if the set of irreps of valence bands can no longer be written as a linear combination of EBRs with non-negative integer coefficients, the material becomes topologically nontrivial. Identifying this scenario is particularly simple if every irrep can be related either to ρ_d or ρ_f, i.e., if these band representations have different irreps. This is, indeed, the case in SmB_6.

III. CUMULATIVE TOPOLOGY IN HEAVY-FERMION INSULATORS

In this section, we discuss the prospect of heavy-fermion insulators to exhibit multiple topological gaps accessible to experimental probes.

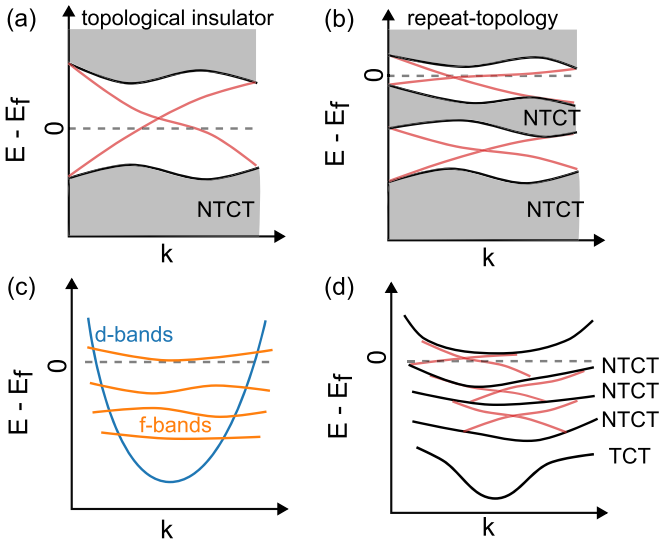

FIG. 2. Schematic figures representing different cases where boundary in-gap states arise. (a) The case of a generic topological insulator. Boundary states populate the gap at E_F due to the nontrivial cumulative topology (NTCT) of the last set of valence bands. (b) Repeat-topological case, where boundary states arise in the gap at E_F and in the next gap below it. (c) Bulk band structure of a heavy-fermion system without hybridization. The region around the Fermi level tends to contain a relatively large number of f bands in such systems. (d) Boundary band structure of a heavy-fermion system with hybridization. The interplay between d and f bands might give rise to a plethora of bands with NTCT whose boundary projections would be connected by in-gap states located close to the Fermi level.

The cumulative topology of a set of bands is defined as the topology of the group formed by these bands and all lower noncore bands. The boundary projections of two separated sets of bulk bands are connected by robust in-gap states if the cumulative topology of the lower set of bulk bands is nontrivial. In particular, a material shows boundary states connecting valence and conduction bands if the cumulative topology of the last set of valence bands is nontrivial, as it is illustrated in Fig. 2(a).

As explained in Ref. [45], the presence of in-gap boundary states is not restricted to the separation between conduction and valence bands. Materials displaying boundary states in the gap at the Fermi level, and in the first gap below it, are dubbed repeat-topological materials [see Fig. 2(b)]. Restricting the definition of repeat topology in Ref. [45] to only two gaps is motivated by the fact that the rest of gaps tend to lie at energies that are hardly accessible for experimental probes like angular-resolved photoemission spectroscopy (ARPES). Nevertheless, materials which exhibit multiple topological gaps could be interesting to explore realizations of multi-gap topology [46–48].

The number of gaps populated with boundary modes accessible to experimental probes might be especially large in the heavy-fermion phases: in these systems, the number of f bands close to E_F tends to be relatively large, as represented in Fig. 2(c). The hybridization between $4f$ and $5d$ bands, as well as between $4f$ bands combined with SOC effects, might

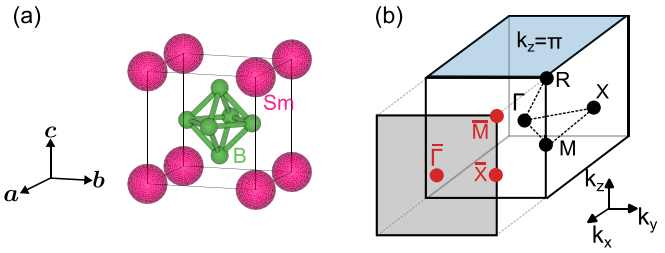

FIG. 3. (a) Primitive unit cell of SmB_6. Sm atoms are shown in magenta (Wyckoff position 1a), while B atoms are shown in green (Wyckoff position 6f). (b) First BZ, where maximal $\boldsymbol{k}$ points are indicated in black. The blue plane is the $k_z = \pi$ plane whose mirror Chern number $C_m|_{k_z=\pi}$ is predicted by the symmetry indicator $z_{4\pi m}$. The gray plane is the BZ of a semi-infinite slab finite along the x axis.

then yield a considerable number of isolated sets of bands with nontrivial cumulative topology close to E_F. According to the discussion above, the boundary projections of these gaps would be connected by in-gap states [see Fig. 2(d)].

IV. SmB_6 REVISITED

SmB_6 crystallizes in a primitive cubic structure in the space group $Pm\bar{3}m$ (No. 221). Our choice of unit cell and BZ are shown in Figs. 3(a) and 3(b), respectively. SmB_6 has been identified as a mixed-valence insulator based on theoretical simulations [24,25] and experimental evidence [26–29]. Furthermore, theoretical analyses predict SmB_6 to be a topological insulator [13,25,35,36]. This prediction is compatible with the robust surface states reported in experimental probes [30–33]. Despite evidence suggesting that the compound is topological, this interpretation is still controversial [49,50]. In this chapter, we revisit the topological classification of SmB_6 in terms of TQC following the analysis introduced in the previous section, and we shed light on the origin of its topology. We support our classification with the analysis of the bulk-boundary correspondence in the crystal, as well as with the study of windings in Wilson loop spectra computed with a minimal TB model that reproduces the topology of the material. Furthermore, we discuss the potential existence of several cumulative-topological bands close to the Fermi level in SmB_6.

A. *Ab initio* band structure and topological classification

The ground state electron density and band structure of SmB_6 have been calculated self-consistently with the Vienna *ab initio* simulation package [51] (VASP). A plane-wave cutoff of 500 eV was used in the self-consistent calculation of the ground-state density and the BZ was sampled with a grid of $9 \times 9 \times 9$. Spin-orbit corrections have been included in the calculations. The general gradient approximation was used for the exchange-correlation term, in the Perdew-Burke-Ernzerhof [52] parametrization. According to our DFT calculations, the average occupation of the $4f$ shell of Sm in the ground state is $n_f = 5.5$, which is in good agreement with previous works [6,24–29,53] SmB_6 is thus a mixed-valence insulator where $4f$ states play the role of localized orbitals, whereas $5d$ states act as overlapping orbitals.

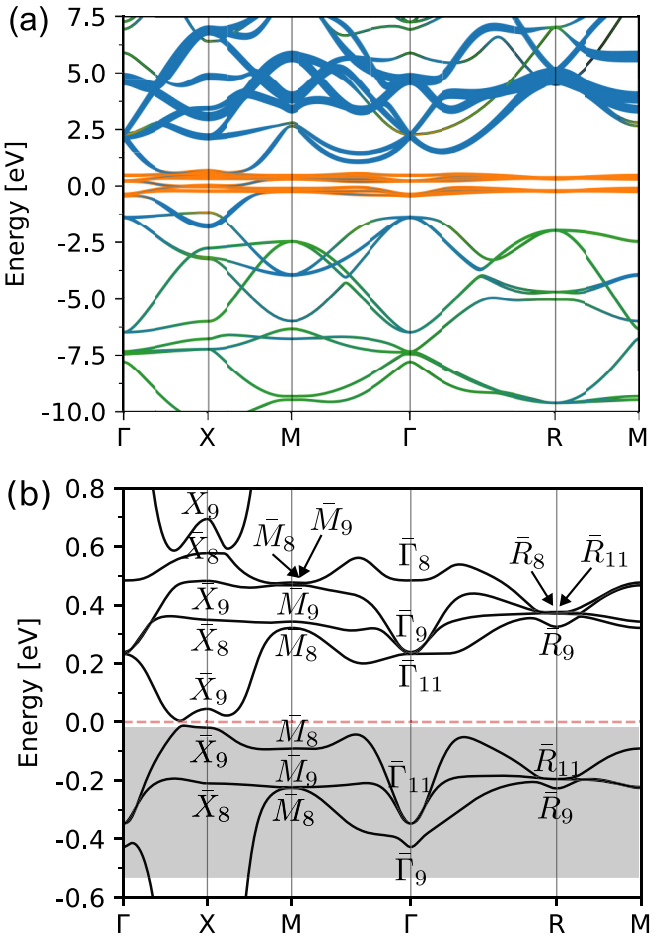

FIG. 4. (a) Band structure of SmB_6 calculated with GGA. Weights of Sm d, Sm f, and B bands are indicated in blue, orange, and green, respectively. (b) $4f$ bands and their little-group irreps. Bands in the grey region correspond to $J = 5/2$ states, while those above the Fermi level stem from $J = 7/2$ states.

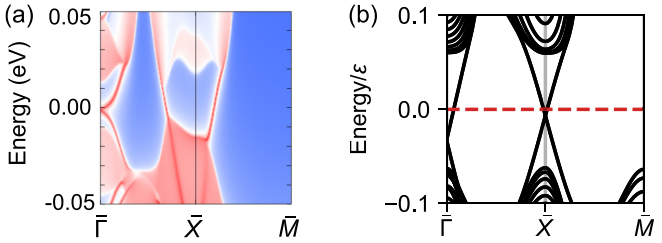

FIG. 5. Surface spectrum of a SmB_6 crystal finite along the x axis. (a) Spectrum calculated via the Wannier TB derived from *ab initio* wave functions. (b) Spectrum computed via the analytical TB model described in Sec. IV C. The energy is provided in terms of the on-site energy ϵ of d orbitals.

Figure 4(a) shows the band structure of SmB_6 and weights of Sm d and f states. Although most $5d$ bands are located above the Fermi level, there is a $5d$ band coming down to -2 eV in the line connecting Γ to X. $4f$ orbitals induce heavy (quasi)bands which lie close to the Fermi level and cut through this $5d$ band, thus the low-energy spectrum is dominated by the presence of $5d$ and $4f$ bands, and the interplay between these bands leads to an insulating band structure. The possibility of having band crossings at $\boldsymbol{k}$ points not represented in the path shown in this figure is analyzed in Appendix C.

In order to determine if the valence bands are topological, we have calculated their little-group irreps at maximal $\boldsymbol{k}$ points of the BZ with the software IRREP [54]. These irreps are shown in Fig. 4(b) for $4f$ bands. It turns out that the set of irreps of valence bands does not coincide with those of any linear combination of EBRs with positive or zero integer coefficients. As a result, SmB_6 is a topological insulator according to the TQC formalism. Furthermore, we have computed the values for the symmetry-based indicators of topology [21,22] corresponding to valence states via the software CHECKTOPOLOGICALMAT [45,55], which yields the $\mathbb{Z}_4$ indicators $z_4 = 1$ and $z_{4\pi m} = 3$, the weak and strong $\mathbb{Z}_2$ indices $(z_{2w,1}, z_{2w,2}, z_{2w,3}; z_2) = (1, 1, 1; 1)$ and the $\mathbb{Z}_8$ index $z_8 = 5$. Whereas the odd value of z_8 identifies the phase as strong topological, the symmetry indicator $z_{4\pi m} = 3$ implies a mirror-Chern number $C_m|_{k_z=\pi} = 3 \mod 4$ in the $k_z = \pi$ plane, i.e., $C_m|_{k_z=\pi} = 1, 3, 5, \ldots$ Therefore the *ab initio* valence bands of SmB_6 host a strong-topological phase, with features of crystalline topology. Our classification is thus able to diagnose in a simple and effective way the features of crystalline topology reported early on by Ye *et al.* [56], and studied in detail by Barusselli and Votja [38], as well as by Legner *et al.* [39].

Figure 5(a) shows the spectral function computed via a Wannier TB model including all Sm $5d$ and $4f$ orbitals as basis states. This model has been constructed via the software WANNIER90 [57]. The surface perpendicular to the x axis exhibits a spectrum with one surface Dirac cone along the $\bar{M}$-$\bar{X}$-$\bar{M}$ line, which is consistent with the value $C_m|_{k_z=\pi} = 1$. In addition, the fact that the number of Dirac cones in the surface BZ is three—hence, it is odd—is compatible with the strong-topology predicted by symmetry indicators [58,59].

Our diagnosis of the topology of SmB_6 is consistent with previous theoretical works which classify the phase as strong topological [13,25,35,36]. We should emphasize that our classification does not diagnose only the strong topology protected by time-reversal symmetry, but also the topology protected by crystalline symmetries.

B. Low-energy physics and origin of the gap

In this section, we follow a group theory and *ab initio* based approach to describe in detail the low-energy part of the band structure of SmB_6. In particular, we identify the most important couplings that contribute to the existence of the gap between valence and conduction states.

The f shell of the isolated Sm atom consists of 14 orbitals transforming as the representation $D_3^- \otimes D_{1/2}^+$ of the symmetry group $O(3)$. Here, D_L^p denotes the irrep of angular momentum L and parity p; for instance, $D_{1/2}^+$ is the spin representation of $O(3)$. However, the representation $D_3^- \otimes D_{1/2}^+$ is reducible and can be decomposed in terms of smaller irreducible representations of $O(3)$

$$D_3^- \otimes D_{1/2}^+(14) = D_{5/2}^-(6) \oplus D_{7/2}^+(8), \tag{1}$$

where $J = 5/2$ and $7/2$ are values for the total-angular momentum, and the dimension of each representation is written within brackets. According to this decompostion, which describes the split produced by SOC from a group theory perspective, the 14-fold degenerate f shell is separated into two groups of 6 and 8 degenerate states. This separation is visible in the band structure shown in Fig. 4(b), where $J = 5/2$ bands are below the Fermi level, while $J = 7/2$ states are above it.

Nevertheless, Sm ions are not isolated in SmB_6, but they are instead surrounded by B and other Sm ions. As a consequence, the symmetry group of every Sm site is reduced from $O(3)$ to its site-symmetry group G_{1a}, which is isomorphic to the point group $m\bar{3}m$. $J = 5/2$ and $J = 7/2$ states transform as the representations of G_{1a} subduced by $D^-_{5/2}$ and $D^-_{7/2}$, which are both reducible and thus decomposable in terms of irreps of the point group

$$D^-_{5/2} \downarrow G_{1a} = \bar{E}_{2u}(2) \oplus \bar{F}_u(4), \tag{2}$$

$$D^-_{7/2} \downarrow G_{1a} = \bar{E}_{2u}(2) \oplus \bar{E}_{1u}(2) \oplus \bar{F}_u(4). \tag{3}$$

This decomposition is the group-theory based analysis of the split of the $4f$ shell of Sm due to the surrounding crystal environment, i.e., the crystal-field splitting. According to it, the $J = 5/2$ set splits into two groups of twofold and fourfold degenerate states, while $J = 7/2$ states separate into a fourfold degenerate and two twofold degenerate sets. As shown in Fig. 4(b), the splitting produced by the crystal environment is not strong enough to modify significantly the band splittings due to SOC. This is a consequence of the small off-site overlaps of $4f$ orbitals due to their spatial localization.

Despite the hybridization between $4f$ states being small compared to SOC, it is enough to prevent a crossing between the highest $J = 5/2$ and lowest $J = 7/2$ bands in the Γ-X line [see Fig. 4(b)]. Without this hybridization SmB_6 would be a metal.

The hybridization between Sm $4f$ and $5d$ orbitals is also essential for the gap between valence and conduction states to be finite, as pointed out in Sec. IV A. In the absence of such hybridization the $5d$ band marked in blue in Fig. 4(a) would not split, and there would be a Fermi surface populated by Bloch states induced from these $5d$ orbitals.

In conclusion, the origin of the spectral gap between valence and conduction states in SmB_6 is governed by the interplay between the strong SOC of Sm, off-site couplings between $4f$ orbitals, and the hybridization of $4f$ states with Sm $5d$ orbitals.

C. Tight-binding model for SmB_6

In this section, we corroborate the value $C_m|_{k_z=\pi} = 1$ for the mirror Chern number of the $k_z = \pi$ plane by analyzing the spectra of Wilson loops. Since accomplishing such an analysis based on *ab initio* calculations is numerically complicated, we construct a minimal symmetry-consistent TB model that reproduces the topology of SmB_6. The model is based on a simplification of the *ab initio* band structure studied in Sec. IV A which, even if less detailed than the original band structure, provides a clear picture of the surface states of the material and their relation to the underlying topology. We will now provide a brief description of the choice of the orbitals for the model. Detailed descriptions of the model and the Hamiltonian can be found in Appendix D.

First, we notice that the irreps at Γ and X of the $5d$ band crossing the Fermi level are $\bar{\Gamma}_{10}$ and $\bar{X}_7$. These irreps coincide with those of the band representation $(\bar{F}_g \uparrow G)_{1a}$ induced from the subset of $5d$ orbitals transforming as the irrep $\bar{F}_g$ of the site-symmetry group G_{1a} of WP 1a. This motivates us to restrict the set of $5d$ orbitals included in the TB model to this set of four states.

To make an efficient choice of $4f$ orbitals, we note that the topology can be explained effectively in terms of a band inversion between $5d$ and $4f$ bands happening at X. The $4f$ band participating in this inversion has irreps $\bar{\Gamma}_{11}$ and $\bar{X}_9$. In fact, these irreps coincide with those of the band representation induced from a subset of $4f$ orbitals transforming as the irrep $\bar{F}_u$ of G_{1a}. The rest of $4f$ bands do not play an essential role in the effective band inversion and can be safely left out of the TB model. Altogether, we consider four $5d$ and four $4f$ orbitals sitting at the site of Sm, which transform as the irreps $\bar{F}_g$ and $\bar{F}_u$ of the site-symmetry group G_{1a}, and induce the elementary band representations $(\bar{F}_g \uparrow G)_{1a}$ and $(\bar{F}_g \uparrow G)_{1a}$, respectively.

In order to determine the value for $C_m|_{k_z=\pi}$, we have analyzed the Wilson loop operator $W(k_y, k_z = \pi)$ defined on the $k_z = \pi$ plane as [60]

$$\begin{aligned} W(k_y, k_z = \pi) &= \prod_{\delta:0\to 2\pi} P_\pi(2\pi - \delta, k_y) \\ &= P_\pi(2\pi, k_y) P_\pi(2\pi - \delta, k_y) \ldots P_\pi(0, k_y), \end{aligned} \tag{4}$$

where δ is a number varying in infinitesimally small steps, and $P_\pi(k_x, k_y) = \sum_n |\psi_n(k_x, k_y, \pi)\rangle\langle\psi_n(k_x, k_y, \pi)|$ is the projector onto valence states at a point $\boldsymbol{k} = (k_x, k_y, \pi)$ of the $k_z = \pi$ plane. The little group of every $\boldsymbol{k}$ point in this plane contains the mirror reflection M_z, whose action on $W(k_y, k_z = \pi)$ is given by

$$M_z W(k_y, k_z = \pi) M_z^{-1} = \prod_{\delta:0\to 2\pi} M_z P_\pi(2\pi - \delta, k_y) M_z^{-1}, \tag{5}$$

where we have inserted the identity $M_z^{-1} M_z = \mathbb{1}$ between every pair of projectors. From the periodicity of Bloch states in reciprocal space it follows that M_z commutes with every projector, $M_z P_\pi(k_x, k_y) M_z^{-1} = P_{-\pi}(k_x, k_y) = P_\pi(k_x, k_y)$. Therefore Eq. (5) reduces to the commutation relation

$$M_z W(k_y, k_z = \pi) M_z^{-1} = W(k_y, k_z = \pi). \tag{6}$$

As a consequence of this relation, it is possible to find a basis of states which are simultaneously eigenstates of M_z and $W(k_y, k_z = \pi)$, and hence the eigenstates of the Wilson loop operator can be separated by their M_z eigenvalue.

Figure 6(a) shows the spectrum of $W(k_y, k_z = \pi)$ calculated with the package PYTHTB [61]. For each eigenvalue of M_z, there is a curve in the spectrum of the Wilson loop which winds once as we go through the plane. Based on the fact that the number of windings in Wilson loop spectra coincides with the mirror-Chern number in this family of topological phases [60,62], the number of windings found here corroborates the mirror-Chern number $C_m|_{k_z=\pi} = 1$ predicted from

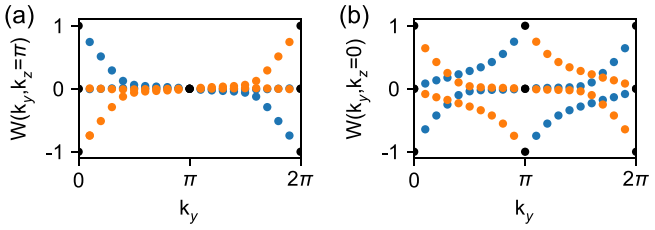

FIG. 6. Mirror-symmetry resolved spectra of Wilson loop operators defined on the (a) $k_z = \pi$ plane and (b) $k_z = 0$ plane. Orange and blue correspond to $+i$ and $-i$ eigenvalues of M_z, respectively.

the symmetry indicators of *ab initio* valence bands [31–33]. Figure 6(b) shows the spectrum of the Wilson loop $W(k_y, k_z = 0)$ on the $k_z = 0$ plane. The number of windings for each subspace of M_z indicates the existence of a mirror Chern number $C_m|_{k_z=0} = 2$, which is consistent with the surface Dirac cones at $\bar{\Gamma}$ and $\bar{X}$ shown in the spectral function in Fig. 5(a).

The TB model derived here has been employed to obtain a simplified picture of the surface state for a crystal finite along the x axis [see Fig. 6(b)]. This surface spectrum is consistent with the spectral function in Fig. 6(a) computed from the *ab initio* band structure, as well as with experimental observations [31–33] and previous theoretical simulations of surface states [14,25,35,36,38,39,56]. This agreement confirms that the TB derived here reproduces both, the bulk topology and bulk-boundary correspondence of SmB_6.

D. Multigap topology in SmB_6

In this section, we comment on the potential of SmB_6 to host multiple topological gaps close to the Fermi level. Since heavy bands tend to be confined in a narrow energy window, gaps separating them are usually small. Hence, their presence in an *ab initio* band structure might depend on the details of the calculation, like the approximation used for the exchange correlation term. For instance, the GGA band structure in Fig. 4 does not display clear multiple topological gaps close to the Fermi level, while the band structure obtained using the modified-Becke-Johnson (MBJ) parametrization [63] in Fig. 7 does (see Appendix B for details).

Both the interplay between $4f$ and $5d$ bands and the topological classification of valence bands are analogous in the electronic structures computed with GGA and MBJ. Moreover, the MBJ spectrum shows close to the Fermi level three gaps separating bands with nontrivial cumulative topology, whose surface projections are expected to host in-gap states. The classification of the topology of these gaps is shown in Table II.

The gap indicated in red separates valence and conduction bands, dictating that valence bands are topological. According to the discussion in Sec. III, since the first gap below the Fermi level (indicated in blue) is also topological, SmB_6 is a repeat-topological material within the MBJ approximation. In addition, the first set of conduction bands also display nontrivial cummulative topology, thus we could also expect the first gap above the Fermi level to exhibit in-gap states. Moreover, the fact that this gap is indirect—i.e., the maximum of the lower band is smaller than the minimum of the band

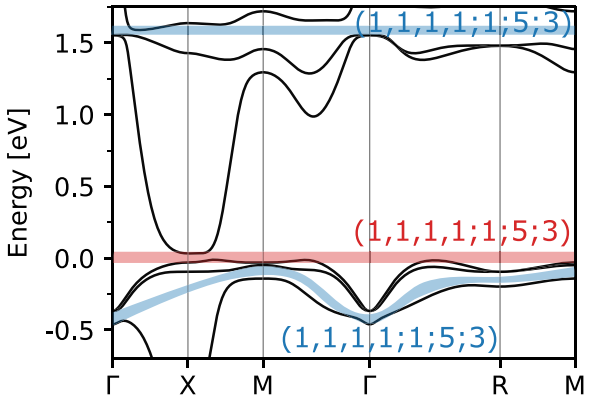

FIG. 7. Band structure of SmB_6 calculated with MBJ functionals. Gaps separating bands with nontrivial cumulative topology from bands above them are indicated in colors. The gap in red separates valence and conduction bands, while blue gaps separate two sets of conduction or valence bands. Cumulative values for the symmetry indicators of topology corresponding to bands below each gap are indicated as $(z_{2w,1}, z_{2w,2}, z_{2w,3}, z_2; z_4; z_{4\pi m}; z_8)$.

on top—makes it a promising testbed for an experimental confirmation of the validity of the single-particle description of SmB_6.

The topological gaps shown in Fig. 7 share the same values for symmetry indicators due to the fact that the irreps of heavy bands involved in the displayed energy range coincide with the irreps of atomic limits coming from $4f$ orbitals. Generally, the interplay between $4f$ bands might lead to heavy bands with nonzero values for the symmetry indicators, which could yield gaps with different topology. These results suggest that SmB_6 might be a promising material to investigate the presence of topological gaps close to the Fermi level.

Different factors might influence the ease to observe in-gap states related to these topological gaps. First, their form and presence on a particular boundary of the crystal might depend on the microscopic details of the actual boundary. In the case of SmB_6 these could be the presence of Sm_2O_3 impurities, the tendency of the B terminated surface to attract—due to electrostatic interaction—Sm atoms forming patterns of altered periodicity, or the difficulty to obtain flat surfaces via cleavage [64–68]. Second, whether in-gap states are isolated from bulk bands might also be important for the possibility of observing these boundary modes. In fact, if the minimum energy of the first band above the gap is smaller than the maximum of the first band below it, the projections of bulk bands on a surface might ovelap and prevent the existence of a spectral gap populated exclusively by boundary in-gap states. Furthermore, some heavy-fermion insulators might show a breakdown of the Kondo coherence [14,69] or present a difference in the valence between the bulk and surface, which might make unclear the manifestation of the bulk-boundary correspondence in these systems.

Although we focused on gaps arising from the interplay between dispersive $5d$ and $4f$ bands—since this is an aspect particular to heavy-fermion systems—the band structure of the material might contain additional topological gaps of different origin. Indeed, the band structure of SmB_6 exhibits

topological bands originating from the interplay between boron bands, as we discuss in Appendix E.

V. DISCUSSION

In this work, we have revisited the topology of SmB_6 within the framework of TQC and symmetry indicators by performing *ab initio* DFT calculations. While state-of-the-art many-body methods beyond DFT provide an accurate description of the electronic properties of SmB_6 [25,36], our DFT calculations also reproduce the mixed-valence behavior of this material, and yield valence bands whose topology is consistent with previous analyses and experimental observations. We have reached a detailed classification of SmB_6 as strong-topological insulator with features of crystalline topology, and constructed a minimal TB model which reproduces the bulk topology, as well as the topological surface states. We have further used this model to corroborate the mirror-Chern number $C_m|_{k_z=\pi} = 1$, and to simulate the surface band structure of the crystal. Our simulations are consistent with ARPES experiments [31–33,70].

Our study suggests that the TQC-based approach might be suitable to achieve a detailed classification of heavy-fermion insulators whose topology exhibits resilience against electron interactions. In fact, this method is capable of diagnosing crystalline topology in an efficient way, in contrast to less general approaches that tend to overlook this type of topology—like those based on the parity or orbital texture of bands. Therefore revisiting heavy-fermion materials within TQC might (1) help diagnosing as topological some phases that had been previously classified as trivial, and (2) unveil the existence of an interplay between crystal symmetries and topology in materials studied previously.

We propose that the framework applied here to look into the topology of heavy-fermion insulators might be suitable for systems whose topology is reproduced within DFT and exhibits robustness under electron interactions. This might include systems where the hybridization between itinerant and localized electrons influences significantly the mixed-valence physics. However, the method might not be suitable for other heavy-fermion systems where the single-particle picture breaks down. For instance, the method might be invalid for quantum phases whose physics is governed by dynamical fluctuations in the occupation of f states, as this phenomenon is out of the scope of DFT. It also remains unexplored the extent to which this approach is applicable to systems where the mixed valence is a consequence of the degeneracy of f-valence states.

Regarding the properties of crystalline topology of SmB_6, although we focused here on the mirror-Chern number that follows directly from the $z_{4\pi m}$ symmetry indicator, the presence of additional topological invariants with nontrivial values cannot be discarded.

Moreover, we have suggested heavy-fermion insulators as potential candidates to host multiple topological in-gap states close to the Fermi level. Based on this suggestion, and the success of our approach in leading to a detailed classification of the topology of valence bands, we hope that the current work might motivate an intesive search of topological phases in heavy-fermion materials. Such a renewed interest could induce the discovery of novel topological materials.

We suggest that the inclusion of magnetic elementary band corepresentations [71] could make the TQC based approach applicable to magnetic topological heavy-fermion materials, as long as their electronic structure can be described in terms of renormalized bands. It remains unexplored to which extent our formalism could be applicable to interacting heavy-fermion phases that are not adiabatically connected to band insulators [72,73].

ACKNOWLEDGMENTS

M.I. thanks S. Wirth, K. Held, M. Votja, and J. Landaeta for enlightening discussions. The work of M.I. was funded by the European Union NextGenerationEU/PRTR-C17.I1, as well as by the IKUR Strategy under the collaboration agreement between Ikerbasque Foundation and DIPC on behalf of the Department of Education of the Basque Government. M.G.V. thanks partial support from the Ministry of Economic Affairs and Digital Transformation of the Spanish Government through the QUANTUM ENIA project call - Quantum Spain project, and by the European Union through the Recovery, Transformation and Resilience Plan - NextGenerationEU within the framework of the Digital Spain 2026 Agenda and European Research Council (ERC) Grant Agreement No. 10102083. M.G.V. and M.I. thanks support to the Spanish Ministerio de Ciencia e Innovacion (Grant No. PID2022-142008NB-I00). M.G.V., R.V., and T.N. acknowledge support of the Deutsche Forschungsgemeinschaft (DFG, German Research Foundation) GA 3314/1-1 -FOR 5249 (QUAST). M.G.V and R.V. are also grateful to the National Science Foundation under Grants No. NSF PHY-1748958 and No. PHY-2309135. The work of J.L.M. has been supported in part by the Basque Government Grant No. IT1628-22 and the PID2021-123703NB-C21 grant funded by MCIN/AEI/10.13039/501100011033/ and by "ERDF a way of making Europe".

APPENDIX A: COMPARISON BETWEEN CLASSIFICATIONS BASED ON SINGLE-PARTICLE AND MULTIPARTICLE STATES

In this section, we will argue that symmetry properties of multiplet and single-particle states close to zero energy are identical in crystals with a shell two electrons short of being half filled. We will follow an approach based on Hund's rules.

Let us consider an atom whose shell of orbital-angular momentum number l is two electrons short from half-filling, i.e., it contains $2l - 1$ electrons, as illustrated in Fig. 8(a). According to Hund's first rule, the multiplet with lowest energy is the one with largest value for the quantum number S of the total spin, which is $S = l - 1/2$ for the case considered here. On the other hand, according to Hund's second rule the multiplet of lowest energy also has the largest allowed value for the total orbital-momentum number L consistent with Hund's first rule, which is $L = 2l - 1$. This combination of spin and orbital momenta leads to a total momentum whose quantum number J could take the values $J = l - 1/2, l + 1/2, \ldots, 3(l - 1/2)$. Hund's third rule states that, for shells with an occupation

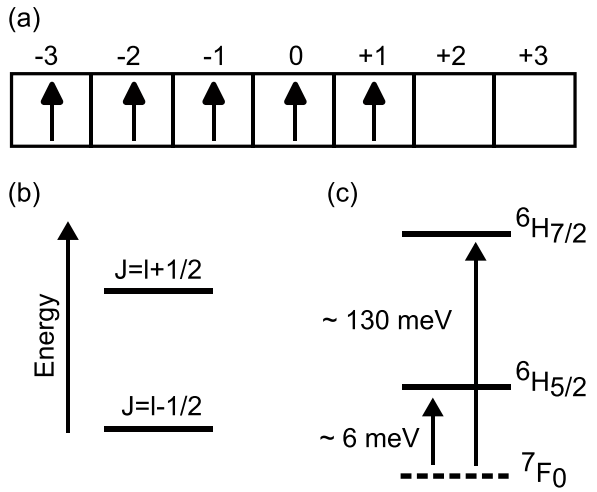

FIG. 8. (a) Diagram for the application of Hund's rules to predict the ground state of a (f-)shell two electrons short from half-filling. (b) Total angular momentum's quantum numbers predicted by Hund's rules for the ground state and first excited state. (c) The case of SmB_6. Solid lines indicate the ground state and first excited multiplet states for an occupation of the f shell two electrons short from half-filling, while the dashed line is the singlet ground-state multiplet of the shell containing six electrons. Binding energies for the transition from the singlet to the multiplets of six electrons are represented [25,28,37,40,74].

smaller than half-filling, the multiplet of lowest energy has in correspondence the minimum value of J. Therefore the term of smallest energy is $J = l - 1/2$. Furthermore, we could expect the first excited state to be $J = l + 1/2$, as it is shown in the diagram of Fig. 8(b).

Regarding single-particle states stemming from the shell of orbital momentum number l, their total angular momentum's quantum number j can take the values $j = l \pm 1/2$. These numbers coincide with those of the two multiplets of lowest energy, and therefore single-particle and multiplet states transform identically under symmetries.

Although this property holds for atoms with a shell two electrons short from half-filling, it is also valid for mixed-valence systems whose spectrum of binding energies is dominated, in the low energy region, by transitions from a singlet to multiplets with this filling. This is indeed the case of SmB_6, where the smallest binding energies correspond to transitions from the singlet ground state $^7F_0$ of $n = 6$ electrons to the multiplet states $^6H_{5/2}$ and $^6H_{7/2}$ of $n = 5$ electrons [25,28,40] [see Fig. 8(c)]. At the same time, single-particle states around the Fermi level are originated from $4f$ orbitals with $l = 3$, thus they are states of $j = 5/2$ and $j = 7/2$ total angular momentum. Multiplets and single-particle states close to zero energy share, therefore, total angular momentum numbers.

The validity of this result relies on the applicability of Hund's rules. We could expect these rules to be valid for lanthanide and actinide elements in mixed-valence and Kondo insulators, as their f shells are well localized deep inside the ions and can not be drastically affected by the crystal environment. Indeed, this is the case for SmB_6 as suggested by the fact that the binding energies calculated in Refs. [25,28,40] for the crystal system are close to those computed in Ref. [74] for isolated Sm^{3+} ions.

APPENDIX B: EFFECT OF STRONG INTERACTIONS

Since SmB_6 is a material where interactions are predicted to be strong, we also calculated the band structure with the Modified-Becke-Johnson (MBJ) parametrization for the exchange-correlation functional [63]. Although heavy-bands occupy a broader range of energy in MBJ band structure, the general features discussed in the main text are identical for both parametrizations. In particular, the interplay between Sm $5d$ and $4f$ bands, and topological classification of valence bands is similar with both parametrizations. We should mention that the bulk band spectrum obtained with MBJ exhibits more separated subsets of bands with nontrivial cumulative topology than the GGA spectrum. The opening of additional gaps upon transitioning from GGA to MBJ is a consequence of the shift of energy levels inherent to the use of a different parametrization for the exchange-correlation energy. Indeed, the use of the MBJ approximation does not produce band inversions responsible for the alteration of the cummulative topology of any gap up to 1.0 eV below the Fermi level.

As shown in Fig. 9, the DOS we computed with GGA resembles the data obtained with LDA in Ref. [25]. Furthermore, the DMFT spectral function is reminiscent of the DOS obtained with DFT, and the main effect of electron interactions is the further flattening of heavy bands around the Fermi level. This results corroborates the fact that the electronic structure of SmB_6 can be described in terms of strongly renormalized heavy and dispersive bands, and encourages us to restrict our numerical analysis to DFT level.

APPENDIX C: EXCLUDING POTENTIAL BAND-CROSSINGS ON HIGH-SYMMETRY LINES, PLANES AND GENERIC POINTS

In this Appendix, we discuss the potential existence of accidental band crossings between valence and conduction bands in SmB_6. For that, we first need to show how symmetries constrain the form of the Hamiltonian on a $\boldsymbol{k}$ point in the BZ.

Let $\hat{H}(\boldsymbol{k})$ be the Hamiltonian operator restricted to bands that potentially cross at particular $\boldsymbol{k}$ point. We consider that the states on these bands transform according to the same physically irreducible representation (pirrep) $D^{\boldsymbol{k}}$, as otherwise they could not hybridize. $\hat{H}(\boldsymbol{k})$ can be written in the following form:

$$\hat{H}(\boldsymbol{k}) = \sum_{ij} h_{ij}(\boldsymbol{k}) |i\rangle\langle j|, \tag{C1}$$

where $|i\rangle$ and $|j\rangle$ run over the states adapted to the symmetry of the pirrep of the bands that (potentially) cross. For a symmetry operation g_k in the little group of $\boldsymbol{k}$ the Hamiltonian must satisfy

$$\begin{aligned} g_{\boldsymbol{k}}^{-1} \hat{H}(\boldsymbol{k}) g_k &= \sum_{ij} h_{ij}(\boldsymbol{k}) g_{\boldsymbol{k}}^{-1} |i\rangle\langle j| g_k \\ &= \sum_{ijmn} h_{ij}(\boldsymbol{k}) [D^{\boldsymbol{k}\dagger}(g_k)]_{mi} |m\rangle\langle n| D^{\boldsymbol{k}}_{jn}(g_k). \end{aligned} \tag{C2}$$

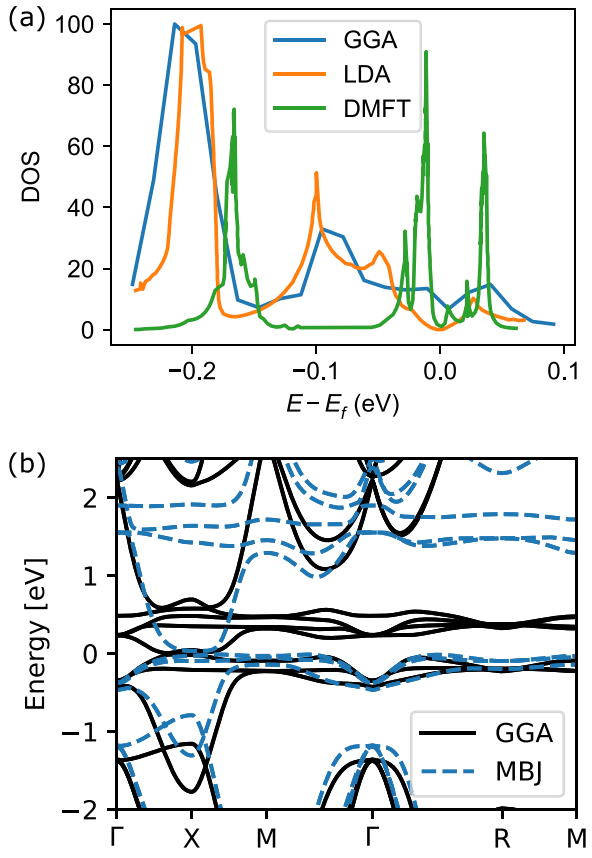

FIG. 9. (a) Comparison between the DOS of the band structure calculated with GGA in the present work (blue), and that computed with the local density approximation (orange) and dynamical mean field theory (green) in Ref. [25]. (b) Comparison between the band structures obtained within GGA and MBJ approximations for the exchange-correlation functional. The separation between $J = 5/2$ and $7/2f$ states is bigger within the MBJ approximation. An increase in the separation between these states was also achieved in Ref. [36] based on the Gutzwiller method. The Fermi level is at zero energy in both figures.

Since $\hat{H}(\boldsymbol{k})$ must commute with all the operations in the little group of $\boldsymbol{k}$, the matrix elements $h_{ij}(\boldsymbol{k})$ must satisfy the following equation:

$$h_{mn}(\boldsymbol{k}) = \sum_{ij} [D^{\boldsymbol{k}\dagger}(g_{\boldsymbol{k}})]_{mi} h_{ij}(\boldsymbol{k}) D^{\boldsymbol{k}}_{jn}(g_{\boldsymbol{k}}). \tag{C3}$$

Equation (C3) might set constrains on the matrix elements $h_{ij}(\boldsymbol{k})$ and therefore describes how crystal symmetries determine the form of $\hat{H}(\boldsymbol{k})$.

Let θ be an antiunitary symmetry in the little group of $\boldsymbol{k}$. The operator in the pirrep $D^{\boldsymbol{k}}$ of such a symmetry can be written as the combination of a unitary matrix U and the complex conjugation operator $\mathcal{K}$, i.e., $D^{\boldsymbol{k}}(\theta) = U\mathcal{K}$. $\hat{H}(\boldsymbol{k})$ should also commute with θ, which imposes the following constrain on the matrix elements $h_{ij}(\boldsymbol{k})$

$$h^*_{mn}(\boldsymbol{k}) = \sum_{ij} U^\dagger_{mi} h_{ij}(\boldsymbol{k}) U_{jn}. \tag{C4}$$

TABLE I. Matrices for the generators of the little cogroup of G_Δ in the representations $\bar{\Delta}_6$ and $\bar{\Delta}_7$.

pirrep	$\{4^+_{010}\|000\}$	$\{m_{001}\|000\}$	$\mathcal{T}\{I\|000\}$
$\bar{\Delta}_6$	$\begin{pmatrix} e^{i3\pi/4} & 0 \\ 0 & e^{-i3\pi/4} \end{pmatrix}$	$\begin{pmatrix} 0 & e^{i\pi/4} \\ e^{i3\pi/4} & 0 \end{pmatrix}$	$\begin{pmatrix} 0 & -1 \\ 1 & 0 \end{pmatrix}$
$\bar{\Delta}_7$	$\begin{pmatrix} e^{-i\pi/4} & 0 \\ 0 & e^{i\pi/4} \end{pmatrix}$	$\begin{pmatrix} 0 & e^{-i3\pi/4} \\ e^{-i\pi/4} & 0 \end{pmatrix}$	$\begin{pmatrix} 0 & -1 \\ 1 & 0 \end{pmatrix}$

In the remaining of this Appendix, we will focus on the line $\Delta(\Gamma X)$ whose points have coordinates $(0, k_y, 0)$. A detailed analysis for the rest of symmetry lines, planes and generic points can be found in Ref. [75]. We will begin deriving the most general form of $\hat{H}(\boldsymbol{k})$ that is compatible with the symmetry of the little group of $\boldsymbol{k}$-points in this line, based on Eqs. (C3) and (C4).

1. Line Δ : $(0, k_y, 0)$

The closing of the gap between valence and conduction bands would involve a touching of states that transform as the pirreps $\bar{\Delta}_6$. We denote $|i\rangle$ and $|j\rangle$ the symmetry-adapted states of one of the Δ_6 pirreps and $|i'\rangle$ and $|j'\rangle$ those of the other Δ_6 pirrep.

Let us consider the matrix elements $h_{ii}(\Delta)$, $h_{ii'}(\Delta)$ and $h_{ij}(\Delta)$ in Eq. (C1). Instead of checking case by case the constrains set by all symmetries in G_Δ, it is sufficient to consider only the action of the generators (see Table I). In particular, applying Eq. (C3) for the fourfold rotation C_{4y} yields

$$h_{ij} = -ih_{ij} \Rightarrow h_{ij} = 0, \tag{C5}$$

and, similarly, $h_{i'j'} = h_{ij'} = h_{i'j} = 0$. The action of the reflection m_z yields

$$\begin{aligned} h_{ii} &= h_{jj}, \\ h_{ii'} &= h_{jj'}. \end{aligned} \tag{C6}$$

together with $h_{i'i'} = h_{j'j'}$ and $h_{i'i} = h_{j'j}$.

As points on the Δ line are not time-reversal invariant, we cannot choose this operation as the antiunitary representative. Nevertheless, we can select the combination of inversion and time-reversal symmetry, i.e., $I\mathcal{T}$, which does belong to the little group. By applying the action of the unitary part U of $I\mathcal{T}$ (see Table I) in Eq. (C4), we obtain the constrain that all matrix elements of $\hat{H}(\Delta)$ must be real functions. Altogether, the most general form of the matrix $H(\Delta)$ compatible with the symmetries in the basis $\{|i\rangle, |i'\rangle, |j\rangle, |j'\rangle\}$ is the following:

$$H(\Delta) = \begin{pmatrix} a(k_y) & b(k_y) & 0 & 0 \\ b(k_y) & a'(k_y) & 0 & 0 \\ 0 & 0 & a(k_y) & b(k_y) \\ 0 & 0 & b(k_y) & a'(k_y) \end{pmatrix}, \tag{C7}$$

where $a(k_y)$, $a'(k_y)$, and $b(k_y)$ are real functions whose particular form depends on the microscopic details of the crystal.

The eigenvalues of this matrix are

$$E_{\pm}(k) = \tfrac{1}{2}[a(k_y) + a'(k_y)] \pm \sqrt{\tfrac{1}{2}[a(k_y) - a'(k_y)]^2 + b^2(k_y)}. \tag{C8}$$

The square root in Eq. (C8) should vanish to have a band crossing. This requires $a(k_y) = a'(k_y)$ and $b(k_y) = 0$ to be satisfied simultaneously. The first condition is met at the intersection k_y of two curves, whereas the second equation defines the point k'_y. The coincidence $k_y = k'_y$ requires fine-tuning of the material's microscopic features, thus it is impossible that two bands that transform as $\bar{\Delta}_6$ cross.

Since the Hamiltonian corresponding to $\bar{\Delta}_7$ bands is identical to Eq. (C7), it is impossible to have a crossing between $\bar{\Delta}_7$ bands without the infinitely accurate tunning of the system's microscopic parameters, which would be unrealistic.

APPENDIX D: CONSTRUCTION OF THE TIGHT-BINDING MODEL

In this section, we describe in detail the construction of the TB model for SmB_6. First, we explain the choice of orbitals, based on the splitting of the $5d$ and $4f$ shells due to the crystal environment and SOC, as well as on the topology of the system.

Let us first focus on the splitting of $5d$ orbitals. In the isolated Sm ion these orbitals transform as the irrep $D_2^+ \otimes D_{1/2}^+$ of the symmetry group $O(3)$. In SmB_6, the tenfold degeneracy of $5d$ orbitals is split due to its surrounding crystal environment and the strong SOC in Sm. This splitting is described from a group theoretical perspective as the decomposition of $D_2^+ \otimes D_{1/2}^+$ into irreps of the site-symmetry group G_{1a} isomorphic to $m\bar{3}m$:

$$D_2^+ \otimes D_{1/2}^+(10) = \bar{E}_{2g}(2) \oplus 2\bar{F}_g(4). \tag{D1}$$

Therefore the $5d$ orbitals separate into a group of twofold and two groups of fourfold degenerate states. Moreover, the little-group irreps $\bar{\Gamma}_{10}$ and $\bar{X}_7$ of the $5d$ band intersected by $4f$ bands coincide with little-group irreps of the band representation $(\bar{F}_g \uparrow G)_{1a}$. The rest of $5d$ bands are too far from the Fermi level to play any role in the topology. This motivates us to restrict the set of $5d$ orbitals included in the TB model to the set of four orbitals transforming as the irrep $\bar{F}_g$ of the site-symmetry group G_{1a}.

To ensure we include the minimal number of $4f$ states needed to reproduce the topology, we note that the contribution of the $5d$ bands to the valence states at high symmetry points is limited to the X point. Moreover, if there were no $5d$ bands close to the Fermi level, the set of valence irreps at X would be $\{\bar{X}_8, 2\bar{X}_9\}$, with $\bar{X}_9$ the irrep of the last valence band. However, due to the interplay between $5d$ and $4f$ bands, the set of valence irreps is $\{\bar{X}_7, \bar{X}_8, \bar{X}_9\}$ instead, with $\bar{X}_7$ coming from the $5d$ bands through the mechanism visualized in Fig. 1. Thus effectively a band inversion has taken place at X such that the irreps $\bar{X}_7$ and $\bar{X}_9$ become part of valence and conduction states, respectively. This observation suggests that the topological phase could be reproduced by considering only the set of $4f$ bands connected to the irrep $\bar{X}_9$. Those bands have the irreps $\bar{\Gamma}_{11}$ at Γ, and the pair $\{\bar{X}_8, \bar{X}_9\}$ at X, and their irreps coincide with those of the band representation $(\bar{F}_u \uparrow G)_{1a}$. We get rid of the rest of $4f$ bands, as they are not essential to reproduce the topology of *ab initio* valence bands. Therefore we restrict the set of $4f$ orbitals included in the TB model to those transforming as the irrep $\bar{F}_u$ of the site-symmetry group G_{1a}.

Altogether, we consider eight spinful Wannier functions sitting at WP 1a. The EBRs $(\bar{F}_g \uparrow G)_{1a}$ and $(\bar{F}_u \uparrow G)_{1a}$ induced from them contain the following little-group irreps at maximal $\boldsymbol{k}$ points

$$(\bar{F}_g \uparrow G)_{1a} : \{\bar{\Gamma}_{10}, \bar{X}_6 \oplus \bar{X}_7, \bar{M}_6 \oplus \bar{M}_7, \bar{R}_{10}\}, \tag{D2}$$

$$(\bar{F}_u \uparrow G)_{1a} : \{\bar{\Gamma}_{11}, \bar{X}_8 \oplus \bar{X}_9, \bar{M}_8 \oplus \bar{M}_9, \bar{R}_{11}\}. \tag{D3}$$

In order to deal efficiently with the constrains set by symmetries on the parameters of the model, and to write down the Hamiltonian, it is convenient to consider the decomposition of these spinful representations as the product of the spin representation $S = \bar{E}_{1g}$ and a spinless representation

$$\bar{F}_g = E_g \otimes S, \tag{D4}$$

$$\bar{F}_u = E_u \otimes S. \tag{D5}$$

Based on these decompositions, we denote the TB basis states $|p_{\boldsymbol{R},i,\sigma}\rangle$, where $\boldsymbol{R}$ is the lattice vector of the unit cell, $p = g, u$ stands for the parity of the corresponding irrep, $i = 1, 2$ labels the state within the basis of the irrep E_p and σ is the spin-degree of freedom—for example, $|g_{\boldsymbol{R},2,\uparrow}\rangle$ is the basis state of $\bar{F}_g$ in the cell $\boldsymbol{R}$ constructed as the product of the second basis state of E_g and the $\uparrow$-spin state. The transformation of these states under a symmetry $h \in m\bar{3}m$ is described by the following expression:

$$h\,|p_{\boldsymbol{R},i,\sigma}\rangle = [E_p(h)]_{i'i} S_{\sigma'\sigma}(h)\,|p_{(h\boldsymbol{R}),i',\sigma'}\rangle\,, \tag{D6}$$

where $E_p(g)$ is the matrix of h in the representation E_p. We will use greek letters to denote the degrees of freedom corresponding to the irreps, except for the parity. The matrix of h in Eq. (D6) will be written accordingly as $V_{\alpha'\alpha} = [E_p(h)]_{i'i} S_{\sigma'\sigma}(h)$, with $\alpha = (i\sigma)$ and $\alpha' = (i'\sigma')$. Then, the matrix elements of the Hamiltonian in the basis of TB states defined in real space can be written as

$$H_{p\alpha,p'\alpha'}(\boldsymbol{R}) = \langle p_{\boldsymbol{R},\alpha}|H|p'_{\boldsymbol{0},\alpha'}\rangle. \tag{D7}$$

Here, we only consider amplitudes for hoppings from the unit cell at the origin. The remaining amplitudes can be related to these through translations by vectors of the lattice. The fact that the Hamiltonian must be invariant under all space-group symmetries, together with Eq. (D6), leads to the following relation between hopping amplitudes:

$$H_{p\beta,p'\beta'}(h\boldsymbol{R}) = V_{\beta\alpha}(h) H_{p\alpha,p'\alpha'}(\boldsymbol{R}) V^{\dagger}_{\alpha'\beta'}(h). \tag{D8}$$

For certain symmetry operations, this relation could further set constrains on some matrix elements, reducing the number of independent parameters needed to describe the considered couplings.

Based on this approach, we have constructed the following symmetry-consistent TB Hamiltonian:

$$
\begin{aligned}
H(\boldsymbol{k}) = &\left[\epsilon_d + t_1 \sum_{i=x,y,z} \cos k_i\right](\nu_0+\nu_3)\otimes\tau_0\otimes\sigma_0 + t_2[\cos(k_x+k_y)+\cos(k_x-k_y)+\cos(k_y+k_z)+\cos(k_y-k_z)+\cos(k_y+k_x)\\
&+\cos(k_y-k_x)](\nu_0+\nu_3)\otimes\tau_0\otimes\sigma_0 + t_3\{\cos(k_x+k_y)+\cos(k_x-k_y)+e^{i2\phi}[\cos(k_y+k_z)+\cos(k_y-k_z)]\\
&+e^{-i2\phi}[\cos(k_y+k_x)+\cos(k_y-k_x)]\}(\nu_0+\nu_3)\otimes\tau_1\otimes\sigma_0 + t_4\{\cos(k_x+k_y)+\cos(k_x-k_y)\\
&+e^{i\phi}[\cos(k_y+k_z)+\cos(k_y-k_z)]+e^{-i\phi}[\cos(k_y+k_x)+\cos(k_y-k_x)]\}(\nu_0-\nu_3)\otimes\tau_1\otimes\sigma_0\\
&+V\sum_i \sin k_i\ \nu_1\otimes\tau_0\otimes\sigma_i. \qquad \text{(D9)}
\end{aligned}
$$

Here ν_i are the Pauli matrices for the d and f sublattice degree of freedom, while τ_i are the Pauli matrices for the states in the basis of irreps E_g and E_u in Eqs. (D4) and (D5), σ_i are the Pauli matrices for spin and $\phi = 4\pi/3$. The term proportional to ϵ_d is the on-site energy of d orbitals, while the origin of energies is chosen so that $\epsilon_f = 0$. The second line in Eq. (D9) represents nearest-neighbor hoppings between d orbitals, the third and fourth lines define next-nearest neighbor (NNN) hoppings between this kind of orbitals, and the fifth line accounts for NNN couplings between f states. Lastly, the term proportional to V is responsible for the hybridization between d and f orbitals. See Appendix D and Fig. 10 for the details of the construction and band structure of the model.

Figure 10 shows the band structure of the TB model, with values for the hopping parameters chosen as to reproduce the ordering of irreps in Fig. 4(b). When the hybridization between $\bar{F}_g$ and $\bar{F}_u$ states is considered ($v > 0$), the first four bands separate from the rest by a gap. The set of irreps of these bands has in correspondence the same values for the symmetry indicators of topology as the *ab initio* valence bands. In particular, they are characterized for having $z_{4\pi m} = 3$ and $z_8 = 5$. Thus the TB model presented here is able to reproduce the topological phase obtained via *ab initio* calculations.

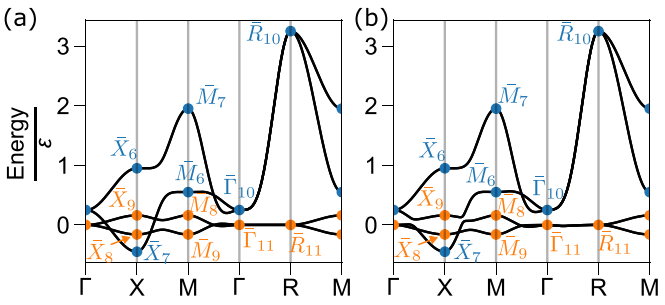

FIG. 10. Tight-binding band structure of SmB_6 with $t_1^{NN}/\epsilon_d = -1/2$, $t_2/\epsilon_d = 1/8$, $t_3/\epsilon_d = 0.7/4$ and $t_4/\epsilon_d = -0.04$. The rest of hopping parameters are chosen to be zero. (a) Bands without hybridization between f and d orbitals. (b) Bands with hybridization $V = 0.06$. Valence bands have in correspondence identical values for symmetry indicators of topology as DFT valence bands calculations.

APPENDIX E: TOPOLOGICAL GAPS BETWEEN VALENCE BANDS IN SmB_6

In the main text, we have focused on the multiple topological gaps that might yield close to the Fermi level the interplay between d and f bands. Nevertheless, the origin of topological gaps is not restricted to these bands. As it is shown in Table II, the gaps between the 27th and 28th bands, as well as the 29th and 30th bands, are also topological. These gaps involve B bands, and are of the order of 1 meV, or even smaller. However, their topology does not contribute to the cumulative topology of the whole set of valence bands, due to the fact that the set of bands coming from B states is completely occupied and has an atomic limit. Moreover, they are gaps located well below the Fermi level, thus accessing them experimentally might be more complicated.

TABLE II. Irreps of the isolated sets of valence bands in the MBJ approximation and their cummulative topology. The first column contains the index of the last band in each set, with the energy increasing with the band number. The last column gives the values for the symmetry indicators of the cummulative topology.

band	Γ	X	M	R	$(z_{2w,1}, z_{2w,2}, z_{2w,3}, z_4, z_2, z_8, z_{4\pi m})$
2	$\bar{\Gamma}_6$	$\bar{X}_6$	$\bar{M}_7$	$\bar{R}_6$	(0, 0, 0, 0, 0, 0, 0)
4	$\bar{\Gamma}_8$	$\bar{X}_8$	$\bar{M}_9$	$\bar{R}_8$	(0, 0, 0, 0, 0, 0, 0)
8	$\bar{\Gamma}_{11}$	$\bar{X}_8$	$\bar{M}_8$	$\bar{R}_{11}$	(0, 0, 0, 0, 0, 0, 0)
		$\bar{X}_9$	$\bar{M}_9$		
22	$\bar{\Gamma}_6$	$\bar{X}_8$	$\bar{M}_6$	$\bar{R}_9$	(0, 0, 0, 0, 0, 0, 2)
	$\bar{\Gamma}_6$	$\bar{X}_6$	$\bar{M}_9$	$\bar{R}_{10}$	
	$\bar{\Gamma}_8$	$\bar{X}_6$	$\bar{M}_8$	$\bar{R}_7$	
	$\bar{\Gamma}_{11}$	$\bar{X}_7$	$\bar{M}_6$	$\bar{R}_8$	
	$\bar{\Gamma}_{10}$	$\bar{X}_8$	$\bar{M}_8$	$\bar{R}_{11}$	
		$\bar{X}_9$	$\bar{M}_7$		
		$\bar{X}_8$	$\bar{M}_7$		
28	$\bar{\Gamma}_{10}$	$\bar{X}_9$	$\bar{M}_6$	$\bar{R}_{10}$	(1, 1, 1, 1, 1, 5, 3)
	$\bar{\Gamma}_7$	$\bar{X}_6$	$\bar{M}_9$	$\bar{R}_7$	
		$\bar{X}_7$	$\bar{M}_8$		
30	$\bar{\Gamma}_9$	$\bar{X}_9$	$\bar{M}_8$	$\bar{R}_9$	(1, 1, 1, 1, 1, 5, 3)
34	$\bar{\Gamma}_{11}$	$\bar{X}_9$	$\bar{M}_9$	$\bar{R}_{11}$	(1, 1, 1, 1, 1, 5, 3)
		$\bar{X}_8$	$\bar{M}_8$		

[1] P.-Y. Chang, O. Erten, and P. Coleman, Möbius Kondo insulators, Nat. Phys. **13**, 794 (2017).

[2] H. Li, Y. Zhong, Y. Liu, H.-G. Luo, and H.-F. Song, $\mathcal{Z}_2$ classification for a novel antiferromagnetic topological insulating phase in three-dimensional topological Kondo insulator, J. Phys.: Condens. Matter **30**, 435601 (2018).

[3] M. Sundermann, F. Strigari, T. Willers, H. Winkler, A. Prokofiev, J. M. Ablett, J.-P. Rueff, D. Schmitz, E. Weschke, M. M. Sala, A. Al-Zein, A. Tanaka, M. W. Haverkort, D. Kasinathan, L. H. Tjeng, S. Paschen, and A. Severing, $CeRu_4Sn_6$: a strongly correlated material with nontrivial topology, Sci. Rep. **5**, 17937 (2015).

[4] P. P. Baruselli and M. Vojta, Scanning tunneling spectroscopy and surface quasiparticle interference in models for the strongly correlated topological insulators SmB_6 and PuB_6, Phys. Rev. B **90**, 201106(R) (2014).

[5] K. Hagiwara, Y. Ohtsubo, M. Matsunami, S.-i. Ideta, K. Tanaka, H. Miyazaki, J. E. Rault, P. L. Fevre, F. Bertran, A. Taleb-Ibrahimi, R. Yukawa, M. Kobayashi, K. Horiba, H. Kumigashira, K. Sumida, T. Okuda, F. Iga, and S.-i. Kimura, Surface Kondo effect and non-trivial metallic state of the Kondo insulator YbB_{12}, Nat. Commun. **7**, 12690 (2016).

[6] A. Menth, E. Buehler, and T. H. Geballe, Magnetic and semiconducting properties of SmB_6, Phys. Rev. Lett. **22**, 295 (1969).

[7] Q. Si and S. Paschen, Quantum phase transitions in heavy fermion metals and Kondo insulators, Phys. Status Solidi B **250**, 425 (2013).

[8] F. Steglich, J. Aarts, C. D. Bredl, W. Lieke, D. Meschede, W. Franz, and H. Schäfer, Superconductivity in the presence of strong pauli paramagnetism: $CeCu_2Si_2$, Phys. Rev. Lett. **43**, 1892 (1979).

[9] N. Grewe and F. Steglich, Chapter 97 Heavy fermions, in *Handbook on the Physics and Chemistry of Rare Earths* (Elsevier, Amsterdam, The Netherlands, 1991), pp. 343–474.

[10] H. Löhneysen, A. Rosch, M. Vojta, and P. Wölfle, Fermi-liquid instabilities at magnetic quantum phase transitions, Rev. Mod. Phys. **79**, 1015 (2007).

[11] R. M. Martin and J. W. Allen, Theory of mixed valence: Metals or small gap insulators (invited), J. Appl. Phys. **50**, 7561 (1979).

[12] P. Coleman, Heavy fermions and the Kondo lattice: a 21st century perspective, arXiv:1509.05769.

[13] M. Dzero, K. Sun, V. Galitski, and P. Coleman, Topological Kondo insulators, Phys. Rev. Lett. **104**, 106408 (2010).

[14] V. Alexandrov, M. Dzero, and P. Coleman, Cubic topological Kondo insulators, Phys. Rev. Lett. **111**, 226403 (2013).

[15] M. Dzero, K. Sun, P. Coleman, and V. Galitski, Theory of topological Kondo insulators, Phys. Rev. B **85**, 045130 (2012).

[16] M. Dzero, J. Xia, V. Galitski, and P. Coleman, Topological Kondo insulators, Annu. Rev. Condens. Matter Phys. **7**, 249 (2016).

[17] M. Klett, S. Ok, D. Riegler, P. Wölfle, R. Thomale, and T. Neupert, Topology and magnetism in the Kondo insulator phase diagram, Phys. Rev. B **101**, 161112(R) (2020).

[18] B. Bradlyn, L. Elcoro, J. Cano, M. G. Vergniory, Z. Wang, C. Felser, M. I. Aroyo, and B. A. Bernevig, Topological quantum chemistry, Nature (London) **547**, 298 (2017).

[19] J. Cano, B. Bradlyn, Z. Wang, L. Elcoro, M. G. Vergniory, C. Felser, M. I. Aroyo, and B. A. Bernevig, Building blocks of topological quantum chemistry: Elementary band representations, Phys. Rev. B **97**, 035139 (2018).

[20] B. Bradlyn, L. Elcoro, M. G. Vergniory, J. Cano, Z. Wang, C. Felser, M. I. Aroyo, and B. A. Bernevig, Band connectivity for topological quantum chemistry: Band structures as a graph theory problem, Phys. Rev. B **97**, 035138 (2018).

[21] H. C. Po, A. Vishwanath, and H. Watanabe, Symmetry-based indicators of band topology in the 230 space groups, Nat. Commun. **8**, 50 (2017).

[22] Z. Song, T. Zhang, Z. Fang, and C. Fang, Quantitative mappings between symmetry and topology in solids, Nat. Commun. **9**, 3530 (2018).

[23] R.-J. Slager, A. Mesaros, V. Juricic, and J. Zaanen, The space group classification of topological band insulators, Nat. Phys. **9**, 98 (2013).

[24] A. Yanase and H. Harima, Band calculations on YbB_{12}, SmB_6 and CeNiSn, Prog. Theor. Phys. Suppl. **108**, 19 (1992).

[25] P. Thunström and K. Held, Topology of SmB_6 determined by dynamical mean field theory, Phys. Rev. B **104**, 075131 (2021).

[26] M. Mizumaki, S. Tsutsui, and F. Iga, Temperature dependence of Sm valence in SmB_6 studied by x-ray absorption spectroscopy, J. Phys.: Conf. Ser. **176**, 012034 (2009).

[27] R. L. Cohen, M. Eibschütz, K. W. West, and E. Buehler, Electronic configuration of SmB_6, J. Appl. Phys. **41**, 898 (1970).

[28] M. Sundermann, H. Yavaş, K. Chen, D. J. Kim, Z. Fisk, D. Kasinathan, M. W. Haverkort, P. Thalmeier, A. Severing, and L. H. Tjeng, $4f$ crystal field ground state of the strongly correlated topological insulator SmB_6, Phys. Rev. Lett. **120**, 016402 (2018).

[29] J.-M. Lee, S.-C. Haw, S.-W. Chen, S.-A. Chen, H. Ishii, K.-D. Tsuei, N. Hiraoka, Y.-F. Liao, K.-T. Lu, and J.-M. Chen, The fluctuating population of Sm 4f configurations in topological Kondo insulator SmB_6 explored with high-resolution x-ray absorption and emission spectra, Dalton Trans. **46**, 11664 (2017).

[30] M. M. Yee, Y. He, A. Soumyanarayanan, D.-J. Kim, Z. Fisk, and J. E. Hoffman, Imaging the Kondo insulating gap on SmB_6, arXiv:1308.1085.

[31] M. Neupane, N. Alidoust, S.-Y. Xu, T. Kondo, Y. Ishida, D. J. Kim, C. Liu, I. Belopolski, Y. J. Jo, T.-R. Chang, H.-T. Jeng, T. Durakiewicz, L. Balicas, H. Lin, A. Bansil, S. Shin, Z. Fisk, and M. Z. Hasan, Surface electronic structure of the topological Kondo-insulator candidate correlated electron system SmB_6, Nat. Commun. **4**, 2991 (2013).

[32] N. Xu, X. Shi, P. K. Biswas, C. E. Matt, R. S. Dhaka, Y. Huang, N. C. Plumb, M. Radović, J. H. Dil, E. Pomjakushina, K. Conder, A. Amato, Z. Salman, D. M. Paul, J. Mesot, H. Ding, and M. Shi, Surface and bulk electronic structure of the strongly correlated system SmB_6 and implications for a topological Kondo insulator, Phys. Rev. B **88**, 121102(R) (2013).

[33] J. Jiang, S. Li, T. Zhang, Z. Sun, F. Chen, Z. R. Ye, M. Xu, Q. Q. Ge, S. Y. Tan, X. H. Niu, M. Xia, B. P. Xie, Y. F. Li, X. H. Chen, H. H. Wen, and D. L. Feng, Observation of possible topological in-gap surface states in the Kondo insulator SmB_6 by photoemission, Nat. Commun. **4**, 3010 (2013).

[34] L. Li, K. Sun, C. Kurdak, and J. W. Allen, Emergent mystery in the Kondo insulator samarium hexaboride, Nat. Rev. Phys. **2**, 463 (2020).

[35] T. Takimoto, SmB_6: A promising candidate for a topological insulator, J. Phys. Soc. Jpn. **80**, 123710 (2011).

[36] F. Lu, J. Z. Zhao, H. Weng, Z. Fang, and X. Dai, Correlated topological insulators with mixed valence, Phys. Rev. Lett. **110**, 096401 (2013).

[37] H. Liu, M. M. Hirschmann, G. A. Sawatzky, G. Khaliullin, and A. P. Schnyder, Correlation induced magnetic topological phases in the mixed-valence compound SmB_6, Phys. Rev. Res. **5**, L042028 (2023).

[38] P. P. Baruselli and M. Vojta, Distinct topological crystalline phases in models for the strongly correlated topological insulator SmB_6, Phys. Rev. Lett. **115**, 156404 (2015).

[39] M. Legner, A. Rüegg, and M. Sigrist, Surface-state spin textures and mirror chern numbers in topological Kondo insulators, Phys. Rev. Lett. **115**, 156405 (2015).

[40] J. D. Denlinger, J. W. Allen, J.-S. Kang, K. Sun, B.-I. Min, D.-J. Kim, and Z. Fisk, SmB_6 photoemission: Past and present, JPS Conf. Proc. **3**, 017038 (2014).

[41] J. Zak, Symmetry specification of bands in solids, Phys. Rev. Lett. **45**, 1025 (1980).

[42] J. Zak, Band representations and symmetry types of bands in solids, Phys. Rev. B **23**, 2824 (1981).

[43] J. Zak, Band representations of space groups, Phys. Rev. B **26**, 3010 (1982).

[44] G. Zwicknagl, Quasiparticles in heavy fermion systems, Phys. Scr. **1993**, 34 (1993).

[45] M. G. Vergniory, B. J. Wieder, L. Elcoro, S. S. P. Parkin, C. Felser, B. A. Bernevig, and N. Regnault, All topological bands of all nonmagnetic stoichiometric materials, Science **376**, (2022).

[46] Q. Wu, A. A. Soluyanov, and T. Bzdušek, Non-abelian band topology in noninteracting metals, Science **365**, 1273 (2019).

[47] B. Lapierre, T. Neupert, and L. Trifunovic, *n* band Hopf insulator, Phys. Rev. Res. **3**, 033045 (2021).

[48] B. Peng, A. Bouhon, R.-J. Slager, and B. Monserrat, Multigap topology and non-abelian braiding of phonons from first principles, Phys. Rev. B **105**, 085115 (2022).

[49] Z.-H. Zhu, A. Nicolaou, G. Levy, N. P. Butch, P. Syers, X. F. Wang, J. Paglione, G. A. Sawatzky, I. S. Elfimov, and A. Damascelli, Polarity-driven surface metallicity in SmB_6, Phys. Rev. Lett. **111**, 216402 (2013).

[50] P. Hlawenka, K. Siemensmeyer, E. Weschke, A. Varykhalov, J. Sánchez-Barriga, N. Y. Shitsevalova, A. V. Dukhnenko, V. B. Filipov, S. Gabáni, K. Flachbart, O. Rader, and E. D. L. Rienks, Samarium hexaboride is a trivial surface conductor, Nat. Commun. **9**, 517 (2018).

[51] G. Kresse and J. Furthmüller, Efficient iterative schemes for *ab initio* total-energy calculations using a plane-wave basis set, Phys. Rev. B **54**, 11169 (1996).

[52] J. P. Perdew, K. Burke, and M. Ernzerhof, Generalized gradient approximation made simple, Phys. Rev. Lett. **77**, 3865 (1996).

[53] H. Hayashi, N. Kanai, N. Kawamura, M. Mizumaki, K. Imura, N. K. Sato, H. S. Suzuki, and F. Iga, A new method for determining the valence of lanthanide compounds: Lγ_4 emission spectroscopy, J. Anal. At. Spectrom. **28**, 373 (2013).

[54] M. Iraola, J. L. Mañes, B. Bradlyn, M. K. Horton, T. Neupert, M. G. Vergniory, and S. S. Tsirkin, IrRep: Symmetry eigenvalues and irreducible representations of *ab initio* band structures, Comput. Phys. Commun. **272**, 108226 (2022).

[55] M. G. Vergniory, L. Elcoro, C. Felser, N. Regnault, B. A. Bernevig, and Z. Wang, A complete catalogue of high-quality topological materials, Nature (London) **566**, 480 (2019).

[56] M. Ye, J. W. Allen, and K. Sun, Topological crystalline Kondo insulators and universal topological surface states of SmB_6, arXiv:1307.7191.

[57] G. Pizzi, V. Vitale, R. Arita, S. Blügel, F. Freimuth, G. Géranton, M. Gibertini, D. Gresch, C. Johnson, T. Koretsune, J. Ibañez-Azpiroz, H. Lee, J.-M. Lihm, D. Marchand, A. Marrazzo, Y. Mokrousov, J. I. Mustafa, Y. Nohara, Y. Nomura, L. Paulatto *et al.*, Wannier90 as a community code: new features and applications, J. Phys.: Condens. Matter **32**, 165902 (2020).

[58] M. Z. Hasan and C. L. Kane, *Colloquium*: Topological insulators, Rev. Mod. Phys. **82**, 3045 (2010).

[59] L. Fu, C. L. Kane, and E. J. Mele, Topological insulators in three dimensions, Phys. Rev. Lett. **98**, 106803 (2007).

[60] B. Bradlyn and M. Iraola, Lecture notes on Berry phases and topology, SciPost Phys. Lect. Notes **51**, (2022).

[61] S. Coh and D. Vanderbilt, Python Tight Binding (PythTB) 1.8.0 (2013).

[62] T. Neupert and F. Schindler, Topological crystalline insulators, in *Topological Matter* (Springer International Publishing, Berlin, Germany, 2018), pp. 31–61.

[63] A. D. Becke and E. R. Johnson, A simple effective potential for exchange, J. Chem. Phys. **124**, 221101 (2006).

[64] P. F. S. Rosa and Z. Fisk, Bulk and surface properties of SmB_6, arXiv:2007.09137.

[65] M. V. A. Crivillero, M. König, J. C. Souza, P. G. Pagliuso, J. Sichelschmidt, P. F. S. Rosa, Z. Fisk, and S. Wirth, Systematic manipulation of the surface conductivity of SmB_6, Phys. Rev. Res. **3**, 023162 (2021).

[66] Y. Ohtsubo, Y. Yamashita, K. Hagiwara, S.-i. Ideta, K. Tanaka, R. Yukawa, K. Horiba, H. Kumigashira, K. Miyamoto, T. Okuda, W. Hirano, F. Iga, and S.-i. Kimura, Non-trivial surface states of samarium hexaboride at the (111) surface, Nat. Commun. **10**, 2298 (2019).

[67] Z. Luo, M. Ferrero, D.-X. Yao, and W. Wu, Inexorable edge Kondo breakdown in topological Kondo insulators, Phys. Rev. B **104**, L161119 (2021).

[68] Y. Ohtsubo, S. ichi Kimura, and F. Iga, Recent progress in clean-surface formation of topological Kondo insulators and topological surface states observed there, Electron. Struct. **4**, 033003 (2022).

[69] V. Alexandrov, P. Coleman, and O. Erten, Kondo breakdown in topological Kondo insulators, Phys. Rev. Lett. **114**, 177202 (2015).

[70] X. Zhang, H. Zhang, J. Wang, C. Felser, and S.-C. Zhang, Actinide topological insulator materials with strong interaction, Science **335**, 1464 (2012).

[71] L. Elcoro, B. J. Wieder, Z. Song, Y. Xu, B. Bradlyn, and B. A. Bernevig, Magnetic topological quantum chemistry, Nat. Commun. **12**, 5965 (2021).

[72] M. Iraola, N. Heinsdorf, A. Tiwari, D. Lessnich, T. Mertz, F. Ferrari, M. H. Fischer, S. M. Winter, F. Pollmann, T. Neupert, R. Valentí, and M. G. Vergniory, Towards a topological

quantum chemistry description of correlated systems: The case of the Hubbard diamond chain, Phys. Rev. B **104**, 195125 (2021).

[73] D. Lessnich, S. M. Winter, M. Iraola, M. G. Vergniory, and R. Valentí, Elementary band representations for the single-particle Green's function of interacting topological insulators, Phys. Rev. B **104**, 085116 (2021).

[74] W. T. Carnall, P. R. Fields, and K. Rajnak, Electronic energy levels in the trivalent lanthanide aquo ions. I. Pr^{3+}, Nd^{3+}, Pm^{3+}, Sm^{3+}, Dy^{3+}, Ho^{3+}, Er^{3+}, and Tm^{3+}, J. Chem. Phys. **49**, 4424 (1968).

[75] M. I. Inurrieta, Topological quantum chemistry description of interacting-electron systems, Ph.D. thesis, University of the Basque Country (2023).